PAPER

Check for updates

From inverse sandwich Ta₂B₇⁺ and Ta₂B₈ to spherical trihedral Ta₃B₁₂⁻: prediction of the smallest metallo-borospherene†

Yu Zhang, Xiao-Yun Zhao, Miao Yan and Si-Dian Li [ID] *

Transition-metal-doped boron nanoclusters exhibit interesting structures and bonding. Inspired by the experimentally discovered inverse sandwich D_{6h} Ta₂B₆ and spherical trihedral D_{3h} La₃B₁₈⁻ and based on extensive first-principles theory calculations, we predict herein the structural transition from perfect di-metal-doped inverse sandwich D_{7h} Ta₂B₇⁺ (**1**) and D_{8h} Ta₂B₈ (**2**) to tri-metal-doped spherical trihedral D_{3h} Ta₃B₁₂⁻ (**3**). As the smallest metallo-borospherene reported to date, Ta₃B₁₂⁻ (**3**) contains three octa-coordinate Ta atoms as integral parts of the cage surface coordinated in three equivalent η⁸-B₈ rings which share two eclipsed equilateral B₃ triangles on the top and bottom interconnected by three B₂ units on the waist. Detailed orbital and bonding analyses indicate that both Ta₂B₇⁺ (**1**) and Ta₂B₈ (**2**) possess σ + π dual aromaticity, while Ta₃B₁₂⁻ (**3**) is σ + π + δ triply aromatic in nature. The IR, Raman, and UV-vis or photoelectron spectra of the concerned species are computationally simulated to facilitate their future spectroscopic characterizations.

1. Introduction

Boron exhibits strong propensity to form multicentre-two-electron bonds (mc-2e bonds) in both polyhedral molecules and bulk allotropes due to its prototypical electron-deficiency.[1–4] Joint photoelectron (PE) spectroscopy experimental and first-principles theory investigations in the past two decades have unveiled a rich landscape for $B_n^{-/0}$ boron nanoclusters from planar or quasi-planar structures ($n = 3$–38, 41–42) to cage-like borospherenes ($n = 39$, 40).[3–7] Cage-like D_{2d} B₄₀⁻/⁰ are the first borospherenes discovered in 2014,[5] while C_3/C_2 B₃₉⁻ are the first axially chiral borospherenes confirmed in experiments as the global minima (GM) of the B_n^- monoanions.[6] These discoveries mark the onset of borospherene chemistry parallel to fullerene chemistry. The borospherene family has been systematically expanded by our group at first-principles theory levels to the cage-like B_n^q series in different charge states ($n = 36$–42, $q = n$–40) which all possess twelve delocalized π bonds on the surface and follow the universal σ + π double delocalization bonding pattern.[5–10] Sea-shell-like C_2 B₂₈⁻/⁰ and C_s B₂₉⁻ were later observed as minor isomers of the monoanions in PES experiments[11,12] and sea-shell-like C_s B₂₉⁺, C_2 B₃₁⁺, C_2 B₃₂, C_2 B₃₄, C_2 B₃₅⁺, and cage-like C_s B₃₉⁺ have also been predicted recently in theory.[13–16]

Institute of Molecular Science, Shanxi University, Taiyuan, 030006, China. E-mail: lisidian@sxu.edu.cn

† Electronic supplementary information (ESI) available. See DOI: 10.1039/d0ra05570k

Transition-metal (TM)-doping induces dramatic structural changes and leads to earlier planar → tubular → spherical structural transitions in boron clusters due to effective TM–B coordination interactions, as evidenced by the experimentally observed pyramidal C_{8v} Ta©B₈⁻,[17] C_s Ta©B₉⁻,[18] and perfect planar D_{10h} Ta©B₁₀⁻ which has the highest coordination number of CN = 10 in planar species[19] and the theoretically predicted half-sandwich TaB₁₂⁻.[20] A family of transition-metal-centred double-ring tubular boron complexes in staggered motifs were recently observed in experiments, including D_{8d} Co@B₁₆⁻,[21] D_{9d} Rh@B₁₈⁻,[22] and C_s Ta@B₂₀⁻,[23] with C_s Ta@B₂₀⁻ (B₂–[Ta@B₁₈]⁻) behaving like a tubular molecular rotor at 900 K facilitated by prototypical multicentre fluxional bonds (FBs) which form and break constantly.[24] A series of perfect di-metal-doped inverse sandwich complexes have also been observed in PE experiments, including D_{6h} Ta₂B₆⁻/⁰,[25] D_{8h} La₂B₈, and D_{8h} Pr₂B₈.[26] Our group recently reported the smallest core-shell-like tubular molecular rotor C_{2h} La₂[B₂@B₁₈] which contains a B₂ core rotating inside a B₁₈ tube almost freely.[27] The first experimentally observed tri-metal-doped inverse triple-decker C_{2v} La₃B₁₄⁻ exhibits a tilted La–B₈–La–B₈–La triple-decker structure with two conjoined η⁸-B₈ rings sharing a B–B unit on one edge.[28] With increasing cluster size, the first perfect spherical trihedral metallo-borospherenes D_{3h} Ln₃B₁₈⁻ (Ln = La, Tb) were very recently discovered in a joint PE experimental and first-principles theory investigation.[29] These metallo-borospherenes represent a new class of unusual geometry with tunable magnetic or catalytic properties, with three deca-coordinate Ln centres as integral parts of the cage surface coordinated in three equivalent η¹⁰-B₁₀ decagons which share two eclipsed

triangular B_6 units interconnected by three B_2 units. Metalloborospherenes were previously proposed in theory for MB_{40} (M = Be, Mg) and Ni_nB_{40} (n = 1–4) which contain hepta-coordinate metal centres on the cage surface of B_{40}, with the corresponding metallo-borophenes with hepta-coordinate metal centres as precursors.[30,31] However, it remains unknown at current stage what is the possible smallest size of metallo-borospherenes and if such coordination-stabilized metallo-borospherenes can be characterized in experiments.

Based on extensive first-principles theory calculations, we predict in this work the possibility of the perfect di-TM-doped inverse sandwich D_{7h} $Ta_2B_7^+$ (**1**) and D_{8h} Ta_2B_8 (**2**) and, more importantly, the smallest tri-TM-doped cage-like metallo-borospherene D_{3h} $Ta_3B_{12}^-$ (**3**) which contains three octa-coordinate Ta centres as integral parts of the cage surface coordinated in three equivalent η^8-B_8 octagons that share two equilateral B_3 triangles interconnected by three B_2 units. Detailed analyses indicate that both $Ta_2B_7^+$ (**1**) and Ta_2B_8 (**2**) are $\sigma + \pi$ dually aromatic in nature, while $Ta_3B_{12}^-$ (**3**) is the first transition-metal-doped boron complex reported to date with $\sigma + \pi + \delta$ triple aromaticity.

2. Theoretical procedure

Extensive global minimum (GM) searches were performed on $Ta_2B_7^+$, Ta_2B_8, and $Ta_3B_{12}^-$ using the Tsinghua Global Minimum (TGMin) package[32,33] based on a constraint Basin-Hopping algorithm,[34] with more than 2000 singlet or triplet stationary points explored for each cluster at PBE/DZVP level.[35] Low-lying isomers were then fully optimized at the PBE0 (36) level with the 6-311+G* basis set[37] for B and Stuttgart relativistic small-core pseudopotential[38,39] for Ta using the Gaussian 16 program suite,[40] with vibrational frequencies checked to make sure that all isomers reported are true minima. The 15 lowest-lying isomers were subsequently fully re-optimized at both PBE0 and BP86 (ref. 41 and 42) levels with the basis sets of aug-cc-pVTZ for B[43,44] and Stuttgart+2f1g for Ta. Relative energies for the four lowest-lying isomers were further refined using the more accurate coupled cluster method with triple excitations CCSD(T)[45–47] implemented in Gaussian 16 with the same basis sets. Natural bonding orbital (NBO) analyses were performed using the NBO 6.0 program[48] and detailed bonding analyses carried out utilizing the adaptive natural density partitioning (AdNDP) approach.[49,50] Molecular dynamics (MD) simulations were performed on $Ta_2B_7^+$ (**1**), Ta_2B_8 (**2**), and $Ta_3B_{12}^-$ (**3**) for 30 ps using the CP2K software suite at different temperatures.[51] The anisotropy of the current-induced density (ACID) analysis[52] was realized using the ACID code, with the ring-current maps generated using POV-Ray 3.7.[53] The iso-chemical shielding surfaces (ICSSs)[54,55] were generated with the Multiwfn 3.7 code.[56] The UV-vis and PES spectra were simulated using the time-dependent TD-DFT-PBE0 approach.[57]

3. Results and discussions

3.1 Structures and stabilities

We start from $Ta_2B_7^+$, the smallest di-metal-doped Ta–B complex concerned in this work. Extensive GM searches

indicate that inverse sandwich D_{7h} $Ta_2B_7^+$ (**1**, $^1A_1$) is the deep-lying GM of the monocation which lies 1.58 eV lower than the second lowest-lying isomer C_{2v} $Ta_2B_7^+$ ($^1A_1$) at CCSD(T) level (Fig. S1†), with the large HOMO–LUMO gap of ΔE_{gap} = 3.77 eV at PBE0. The monocation contains a perfect B_7 ring sandwiched between two Ta atoms along the C_7 molecular axis at the two ends (similar to the experimentally observed inverse sandwich D_{6h} Ta_2B_6 which has a perfect B_6 ring sandwiched between two Ta atoms[24]), with the B–B bond length of r_{B-B} = 1.54 Å, Ta–B distance of r_{Ta-B} = 2.28 Å, and Ta–Ta distance of r_{Ta-Ta} = 2.86 Å (which is obviously larger than the proposed Ta–Ta single bond length of 2.46 Å[58]). With one more B atom added in, the perfect inverse sandwich D_{8h} Ta_2B_8 (**2**, $^1A_{1g}$) is achieved which is the deep-lying GM of the neutral lying 0.62 eV lower in energy than the second lowest-lying isomer C_s Ta_2B_8 ($^1A'$) at CCSD(T) (Fig. S2†). It encompasses a perfect B_8 ring sandwiched between two Ta atoms along the C_8 molecular axis at the two ends, with the HOMO–LUMO gap of ΔE_{gap} = 2.15 eV at PBE0. With a B_8 octagon as the ligand, the Ta–Ta distance in Ta_2B_8 (**2**) is effectively shortened to r_{Ta-Ta} = 2.52 Å which is close to the proposed average Ta–Ta single bond length.[58] The highly stable inverse sandwich $Ta_2B_7^+$ (**1**) and Ta_2B_8 (**2**) may serve as building blocks to form tri-metal-doped Ta–B complexes, similar to the situation in the experimentally observed triple-decker C_{2v} $La_3B_{14}^-$ (28) and spherical trihedral D_{3h} $La_3B_{18}^-$.[29]

Following the direction, we obtained the lowest-lying C_{2v} $Ta_3B_{10}^+$ ($^1A_1$) for $Ta_3B_{10}^+$, C_s $Ta_3B_{11}^-$ ($^1A'$) for $Ta_3B_{11}^-$, and C_s $Ta_3B_{11}^-$ ($^2A'$) for $Ta_3B_{11}^-$ which all possess incomplete spherical-trihedral structures with one edge broken (Fig. S3†). The smallest perfect spherical trihedron was achieved at D_{3h} $Ta_3B_{12}^-$ (**3**, $^1A_1'$) which, as the GM of the monoanion, lies 0.24 eV lower than the second lowest-lying C_{2v} $Ta_3B_{12}^-$ ($^1A_1$) and 1.06 eV lower than the third lowest-lying C_s $Ta_3B_{12}^-$ ($^1A'$) (which both belong to metallo-borospherenes) at the most reliable CCSD(T) level (Fig. S4†). As shown in Fig. 1, $Ta_3B_{12}^-$ (**3**) contains three equivalent octa-coordinate Ta centres as integral parts of the cage surface coordinated in three equivalent η^8-B_8 rings which share two eclipsed equilateral B_3 triangles at the top and bottom interconnected by three B_2 units on the waist. It has the calculated B–B bond lengths of r_{B-B} = 1.58–1.74 Å, Ta–B coordination distances of r_{Ta-B} = 2.26–2.27 Å, and elongated Ta–Ta distances
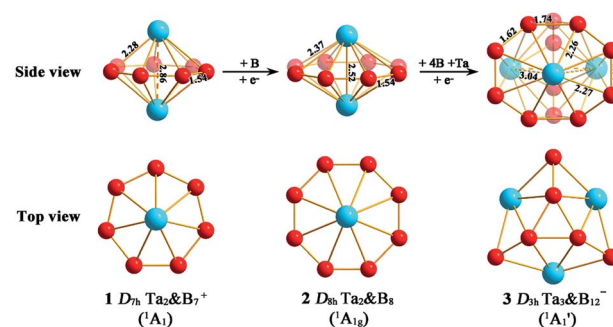

Fig. 1 Optimized structures of D_{7h} $Ta_2B_7^+$ (**1**), D_{8h} Ta_2B_8 (**2**), and D_{3h} $Ta_3B_{12}^-$ (**3**) at PBE0//B/aug-cc-pVTZ/Ta/Stuttgart+2f1g level, with bond lengths indicated in Å.

of r_{Ta-Ta} = 3.04 Å, respectively, with the large HOMO(e'')–LOMO(e') gap of ΔE_{gap} = 2.50 eV at PBE0 which is comparable with the corresponding value of 2.70 eV calculated for the experimentally observed D_{3h} La$_3$B$_{18}^-$ (29) at the same theoretical level. Ta$_3$B$_{12}^-$ (3) can be constructed from Ta$_2$B$_8$ (2) by adding one B$_4$ edge ($\supset$B–B–B–B$\subset$) perpendicular to the B$_8$ ring in the front and one Ta atom coordinated to the newly formed B$_8$ ring, forming three interconnected Ta$_2$B$_8$ inverse sandwiches around the C_3 main molecular axis (Fig. 1). In comparison with D_{3h} Ln$_3$B$_{18}^-$ (Ln = La, Tb) which possess a perfect cage-like D_{3h} B$_{18}$ ligand with three equivalent η^{10}-B$_{10}$ decagons sharing two eclipsed B$_6$ triangles at the top and bottom interconnected by three B$_2$ units on the waist,[29] Ta$_3$B$_{12}^-$ (3) has a perfect cage-like D_{3h} B$_{12}$ ligand with three equivalent η^8-B$_8$ octagons sharing two eclipsed B$_3$ triangles at the top and bottom interconnected by three B$_2$ units on the waist. Ta$_3$B$_{12}^-$ (3) has the same symmetry (D_{3h}) as Ln$_3$B$_{18}^-$, but smaller in size with six less B atoms in the ligand. Such a structural change can be understood based on the fact that Ta ([Xe]5d^{3}6s^2) has a smaller atomic radius (1.46 Å) than that (1.83 Å) of La ([Xe]5d^{1}6s^2),[59] but possesses two more 5d valence electrons than the latter. The Ta centres appear to have the right atomic radii and electronic configurations to match the D_{3h} B$_{12}$ ligand both electronically and geometrically. Ta$_3$B$_{12}^-$ (3) is therefore the smallest metallo-borospherene reported to date. Perfect spherical trihedral D_{3h} Nb$_3$B$_{12}^-$ and D_{3h} V$_3$B$_{12}^-$ also appear to be true minima of the systems at both PBE0 and BP86 levels (Fig. S5†), with the HOMO–LUMO gaps of ΔE_{gap} = 2.59 and 2.67 eV at PBE0, respectively.

Extensive MD simulations (Fig. S6†) indicate that Ta$_2$B$_7^+$ (1), Ta$_2$B$_8$ (2), and Ta$_3$B$_{12}^-$ (3) are dynamically stable at 1200 K, 700 K, and 1200 K, with the small calculated average root-mean-square-deviations of RMSD = 0.11, 0.10, and 0.11 Å and maximum bond length deviations of MAXD = 0.27, 0.24, and 0.29 Å, respectively. No high-lying isomers were observed during the MD simulation. Ta–B complexes with larger HOMO–LUMO energy gaps appear to be dynamically more stable than the ones with narrower energy gaps.

3.2 Natural orbital and bonding analyses

The high stabilities of these high-symmetry complexes originate from their unique electronic structures and bonding patterns. Detailed natural bonding orbital (NBO) analyses show that the Ta centres in Ta$_2$B$_7^+$ (1), Ta$_2$B$_8$ (2), and Ta$_3$B$_{12}^-$ (3) possess the electronic configurations of Ta [Xe]6s$^{0.21}$5d$^{3.46}$, Ta [Xe] 6s$^{0.22}$5d$^{3.64}$, and Ta [Xe]6s$^{0.24}$5d$^{3.72}$, natural atomic charges of q_{Ta} = +1.34|e|, +1.12|e| and +1.01|e|, and total Wiberg bond indexes of WBI$_{Ta}$ = 4.85, 4.80, and 5.07, respectively, indicating that each Ta centre in these complexes donates its 6s^2 electrons almost completely to the B$_n$ ligand (n = 7, 8, 12), while, in return, accepts roughly one electron in its partially filled 5d orbitals from the B$_n$ ligands via p → d back-donations. The formations of effective Ta–B coordination interactions in 1–3 are strongly supported by the calculated Ta–B bond orders of WBI$_{Ta-B}$ = 0.59, 0.40, and 0.50–0.53 (Ta–B interactions within TaB$_7$ or TaB$_8$ pyramids) which appear to be systematically higher than the typical Cr–C coordination bond orders of

WBI$_{Cr-C}$ = 0.34 in D_{6h} Cr(C$_6$H$_6$)$_2$. As mentioned above, a Ta centre in Ta$_3$B$_{12}^-$ (3) has the total bond order of WBI$_{Ta}$ = 5.07 which is also obviously higher than the corresponding value of WBI$_{Cr}$ = 4.12 calculated for Cr in D_{6h} Cr(C$_6$H$_6$)$_2$.

Detailed AdNDP bonding analyses unveil both the localized and delocalized bonds of the concerned systems. As shown in Fig. 2a, Ta$_2$B$_8$ (2) possesses 8 2c–2e B–B σ bonds on the periphery of the η^8-B$_8$ ligand with the occupation numbers of ON = 1.82|e| and 1 2c–2e Ta–Ta σ bond between the two Ta centres with ON = 2.00|e| in the first row. The remaining 16 valence electrons form 8 totally delocalized 10c–2e coordination bonds between the η^8-B$_8$ ligand and two Ta coordination centres with ON = 2.00|e|, including 3 10c–2e σ bonds in the second row, 3 10c–2e π bonds in the third row, and 2 10c–2e (p–d) δ bonding interactions in the fourth row. Both the

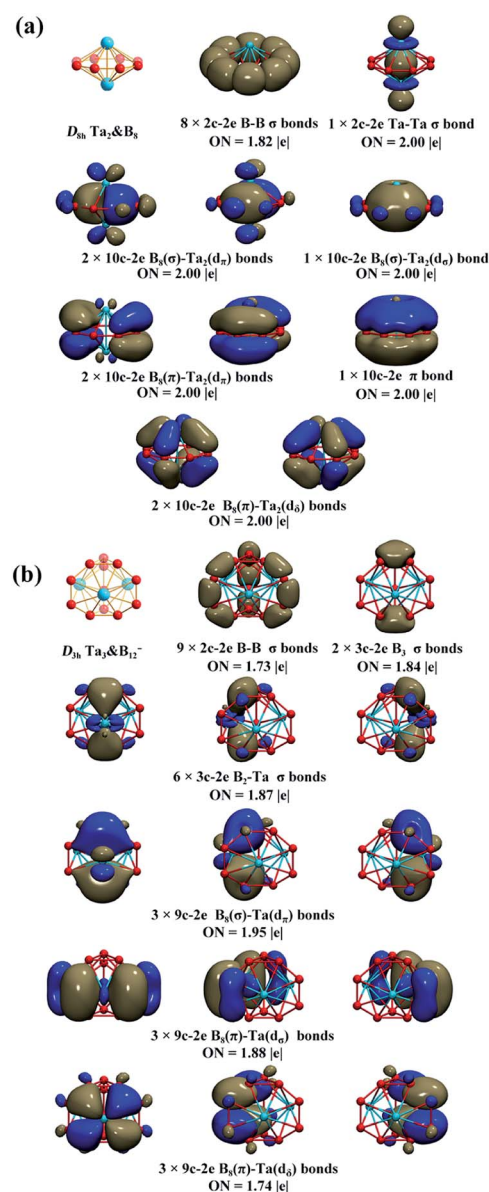**Fig. 2** AdNDP bonding patterns of (a) D_{8h} Ta$_2$B$_8$ (2) and (b) D_{3h} Ta$_3$B$_{12}^-$ (3), with the occupation numbers (ON) indicated.

delocalized 6e σ-system and delocalized 6e π-system match the $4n + 2$ aromatic rule ($n = 1$) and together they render σ + π dual aromaticity to Ta_2B_8 (**2**). Similarly, both the experimentally observed D_{6h} Ta_2B_6 (ref. 25) and D_{7h} $Ta_2B_7^+$ (**1**) are σ + π doubly aromatic in nature, as clearly indicated in their canonical molecular orbitals (CMOs) depicted in Fig. S7.†

The AdNDP bonding pattern of spherical trihedral $Ta_3B_{12}^-$ (**3**) (Fig. 2b) exhibits certain similarity with that of the inverse sandwich Ta_2B_8 (**2**), but it is more complex and intriguing. $Ta_3B_{12}^-$ (**3**) possesses 9 localized 2c–2e σ B–B bonds in the three B_2 units and between the B_2 units and the six apexes of the two B_3 triangles and 2 equivalent 3c–2e σ bonds on the two B_3 triangles at the top and bottom in the first row and 6 equivalent 3c–2e B_2–Ta σ bonds between the three Ta atoms and the two B_3 triangles at the top and bottom in the second row. The remaining 18 valence electrons form 9 delocalized 9c–2e bonds evenly distributed on three equivalent C_{2v} TaB_8 octagonal pyramids (which are similar to the experimentally observed C_{8v} TaB_8^- octagonal pyramid[17]) around the C_3 main molecular axis, including 3 equivalent 9c–2e $B_8(\sigma)$–$Ta(d_\pi)$ bonds in the third row, 3 equivalent 9c–2e $B_8(\pi)$–$Ta(d_\sigma)$ bonds in the fourth row, and 3 equivalent $B_8(\pi)$–$Ta(d_\delta)$ bonds in the fifth row. Each Ta&B_8 octagonal pyramid thus possesses 1 9c–2e $B_8(\sigma)$–$Ta(d_\pi)$ bond, 1 9c–2e $B_8(\pi)$–$Ta(d_\sigma)$ bond, and 1 $B_8(\pi)$–$Ta(d_\delta)$ bond. Overall, the Ta_3&B_{12}^- (**3**) spherical trihedron has 3 equivalent (d–p)σ bonds, 3 equivalent (d–p)π bonds, and 3 equivalent (d–p)δ bonds evenly distributed on three equivalent Ta&B_8 octagonal pyramids around the C_3 molecular axis, forming one delocalized 6e σ-system, one delocalized 6e π-system, and one delocalized 6e δ-system on the cage surface each matching the $4n + 2$ rule ($n = 1$) independently. Such a delocalized bonding pattern renders σ + π + δ triple aromaticity to the smallest metallo-borosphere of $Ta_3B_{12}^-$ (**3**) which is a highly stable D_{3h} spherical trihedron with 18 delocalized electrons evenly distributed on the cage surface.[60]

The aromatic nature of $Ta_2B_7^+$ (**1**), Ta_2B_8 (**2**), and $Ta_3B_{12}^-$ (**3**) is further evidenced by their calculated nucleus-independent chemical shift (NICS) values of NICS = −110.5, −101.9, and −86.6 ppm at the geometrical centres, respectively. Based on the calculated NICS-ZZ components, Fig. 3 plots their iso-chemical-shielding surfaces[54,55] with Z-axis parallel to the designated C_7, C_8, or C_2 molecular axes to illuminate the chemical shielding around the TaB_7 or TaB_8 pyramids in these complexes. Obviously, the space inside the spherical trihedron surrounded by the delocalized Ta–B_n coordination bonds in horizontal direction or within about 1.0 Å above the Ta centres in vertical direction belong to chemical shielding regions (highlighted in yellow) with negative NICS-ZZ values, indicating that the aromatic contribution mainly comes from Ta(5d)–B(2p) coordination interactions between the Ta centres and B_n ligands around them ($n = 7$ or 8), while the chemical de-shielding areas (highlighted in green) with positive NICS values are located outside the B_n ring in horizontal direction. The ICSSs of these complexes appear to be analogous to that of the prototypical aromatic benzene.[54–56]

Fig. S8† depicts the corresponding ring current maps of $Ta_2B_7^+$ (**1**), Ta_2B_8 (**2**), and $Ta_3B_{12}^-$ (**3**). Consistent magnetic
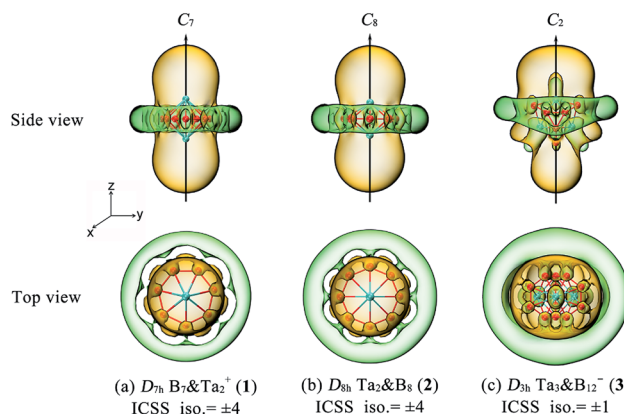

Fig. 3 Calculated iso-chemical shielding surfaces (ICSSs) of (a) $Ta_2B_7^+$ (**1**), (b) Ta_2B_8 (**2**), and (c) $Ta_3B_{12}^-$ (**3**), with the corresponding NICS-ZZ components indicated. The C_7 axis of $Ta_2B_7^+$ (**1**), C_8 axis of Ta_2B_8 (**2**), and C_2 axis of $Ta_3B_{12}^-$ (**3**) are designated as z axis in vertical direction to compare the shielding effects around the TaB_n pyramids ($n = 7, 8$). Yellow regions stand for chemical shielding areas, while green areas represent chemical de-shielding areas.

responses occur in **1**, **2**, and **3** in an external magnetic field in the vertical direction parallel to the assigned molecular axes, irrespective of the electron type, similar to the situations in both benzene[52,53] and double-ring tubular B_{20} (61) which are known to possess typical planar or tubular aromaticity. Such diatropic ring currents well support the aromatic nature of these Ta-doped boron complexes.

3.3 Simulated IR, Raman, and PE spectra of $Ta_3B_{12}^-$ (**3**)

We computationally simulate the IR, Raman, and UV-vis or PES spectra of $Ta_2B_7^+$ (**1**), Ta_2B_8 (**2**), and $Ta_3B_{12}^-$ (**3**) at PBE0 level to facilitate their future spectral characterizations. PE measurements and infrared photodissociation (IR-PD) spectra in combination with first-principles theory calculations have proven to be powerful approaches in characterizing novel clusters in gas phases.[3–7,17–28,62] As shown in Fig. 4, the high-symmetry $Ta_3B_{12}^-$ (**3**) exhibits relatively simple IR and Raman spectral patterns, with the major IR active peaks at 507 (e′), 559 (e′), 668 (a_2''), and 881 (e′) cm^{-1} (Fig. 4a) and main Raman spectral features at 209 (a_1'), 881 (e′), 998 (e″), and 1201 (a_1') cm^{-1} (Fig. 4b), respectively. The first Raman active symmetrical vibrational mode (a_1') at 209 cm^{-1} corresponds to typical "radial breathing mode" (RBM) of the metallo-borosphere which may be used to characterize the hollow structures of single-walled boron nanoclusters in experiments.[63]

The calculated PE spectrum of $Ta_3B_{12}^-$ (**3**) in Fig. 4c exhibits major spectral features at 2.95 ($^2E''$), 3.17 ($^2A_1'$), 3.66 ($^2A_2''$), 3.98 ($^2E'$), 4.17 ($^2A_1''$), 5.32 ($^2E'$), 5.68 ($^2E'$), and 5.98 ($^2A_2''$), respectively, corresponding to vertical electronic transitions from the ground state of the anion ($^1A_1'$) to the excited states of the neutral at the ground-state geometry of the anion. The open-shell neutral Ta_3B_{12} has a slightly distorted C_{2v} Ta_3B_{12} ($^2A_2$) ground-state structure due to Jahn–Teller effect, with the calculated electron affinity of EA = 2.87 eV. The simulated IR, Raman, and UV-vis spectra of $Ta_2B_7^+$ (**1**) and Ta_2B_8 (**2**) are depicted in Fig. S9.†
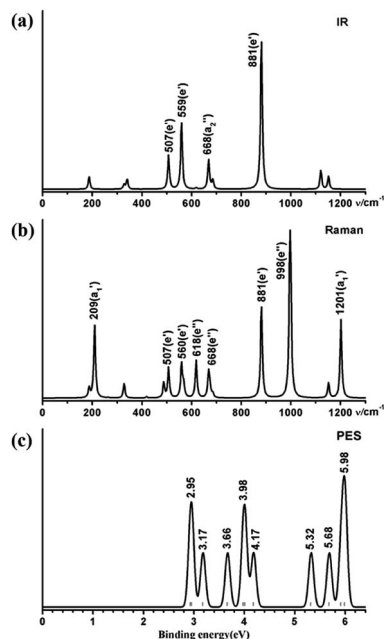
Fig. 4 Simulated (a) IR, (b) Raman, and (c) PES spectra of D_{3h} $Ta_3B_{12}^-$ (3) at PBE0//B/aug-cc-pVTZ/Ta/Stuttgart+2f1g level.

4.   Conclusions

Extensive first-principles theory calculations performed in this work indicate a structural transition from perfect inverse sandwich D_{7h} $Ta_2B_7^+$ (1) and D_{8h} Ta_2B_8 (2) to the smallest metallo-borospherene D_{3h} $Ta_3B_{12}^-$ (3). As the first transition-metal-doped boron complex reported to date with $\sigma + \pi + \delta$ triple aromaticity, $Ta_3B_{12}^-$ (3) possesses three octa-coordinate Ta centres as integral parts of the cage surface coordinated in three equivalent η^8-B_8 octagons. The results obtained in this work suggest that a large family of coordination-stabilized multi-TM-doped TM_mB_n metallo-borospherenes with tunable magnetic and electronic properties may exist in experiments in which the transition metal dopants and B_n ligands match both geometrically and electronically.

Conflicts of interest

There are no conflicts to declare.

Acknowledgements

Notes and references

1 W. N. Lipscomb, *Science*, 1977, **196**, 1047.
2 F. A. Cotton, G. Wilkinson, C. A. Murillo, and M. Bochmann, *Advanced Inorganic Chemistry*, Wiley, New York, 6th edn, 1999.
3 L. S. Wang, *Int. Rev. Phys. Chem.*, 2016, **35**, 69.
4 T. Jian, X. N. Chen, S. D. Li, A. I. Boldyrev, J. Li and L. S. Wang, *Chem. Soc. Rev.*, 2019, **48**, 3550.
5 H. J. Zhai, Y. F. Zhao, W. L. Li, Q. Chen, H. Bai, H. S. Hu, Z. A. Piazza, W. J. Tian, H. G. Lu, Y. B. Wu, Y. W. Mu, G. F. Wei, Z. P. Liu, J. Li, S. D. Li and L. S. Wang, *Nat. Chem.*, 2014, **6**, 727.
6 Q. Chen, W. L. Li, Y. F. Zhao, S. Y. Zhang, H. S. Hu, H. Bai, H. R. Li, W. J. Tian, H. G. Lu, H. J. Zhai, S. D. Li, J. Li and L. S. Wang, *ACS Nano*, 2015, **9**, 754.
7 Q. Chen, S. Y. Zhang, H. Bai, W. J. Tian, T. Gao, H. R. Li, C. Q. Miao, Y. W. Mu, H. G. Lu, H. J. Zhai and S. D. Li, *Angew. Chem., Int. Ed.*, 2015, **54**, 8160.
8 Q. Chen, H. R. Li, C. Q. Miao, Y. J. Wang, H. G. Lu, Y. W. Mu, G. M. Ren, H. J. Zhai and S. D. Li, *Phys. Chem. Chem. Phys.*, 2016, **18**, 11610.
9 W. J. Tian, Q. Chen, H. R. Li, M. Yan, Y. W. Mu, H. G. Lu, H. J. Zhai and S. D. Li, *Phys. Chem. Chem. Phys.*, 2016, **18**, 9922.
10 Q. Chen, H. R. Li, W. J. Tian, H. G. Lu, H. J. Zhai and S. D. Li, *Phys. Chem. Chem. Phys.*, 2016, **18**, 14186.
11 Y. J. Wang, Y. F. Zhao, W. L. Li, T. Jian, Q. Chen, X. R. You, T. Ou, X. Y. Zhao, H. J. Zhai, S. D. Li, J. Li and L. S. Wang, *J. Chem. Phys.*, 2016, **144**, 064307.
12 H. R. Li, T. Jian, W. L. Li, C. Q. Miao, Y. J. Wang, Q. Chen, X. M. Luo, K. Wang, H. J. Zhai, S. D. Li and L. S. Wang, *Phys. Chem. Chem. Phys.*, 2016, **18**, 29147.
13 L. Pei, H. R. Li, M. Yan, Q. Chen, Y. W. Mu, H. G. Lu, Y. B. Wu and S. D. Li, *Phys. Chem. Chem. Phys.*, 2018, **20**, 15330.
14 L. Pei, M. Yan, X. Y. Zhao, Y. W. Mu, H. G. Lu, Y. B. Wu and S. D. Li, *RSC Adv.*, 2020, **10**, 10129.
15 H. Liu, Q. Chen, H. R. Li, X. Y. Zhao, X. X. Tian, Y. W. Mu, H. G. Lu and S. D. Li, *Phys. Chem. Chem. Phys.*, 2018, **20**, 15344.
16 X. Y. Zhao, Q. Chen, H. R. Li, Y. W. Mu, H. G. Lu and S. D. Li, *Phys. Chem. Chem. Phys.*, 2017, **19**, 10998.
17 W. L. Li, A. S. Ivanov, J. Federič, C. Romanescu, I. Černušák, A. I. Boldyrev and L. S. Wang, *J. Chem. Phys.*, 2013, **139**, 104312.
18 C. Romanescu, T. R. Galeev, W. L. Li, A. I. Boldyrev and L. S. Wang, *J. Chem. Phys.*, 2013, **138**, 134315.
19 T. R. Galeev, C. Romanescu, W. L. Li, L. S. Wang and A. I. Boldyrev, *Angew. Chem., Int. Ed.*, 2012, **51**, 2101.
20 B. L. Chen, W. G. Sun, X. Y. Kuang, C. Lu, X. X. Xia, H. X. Shi and G. Maroulis, *Inorg. Chem.*, 2018, **57**, 343.
21 I. A. Popov, T. Jian, G. V. Lopez, A. I. Boldyrev and L. S. Wang, *Nat. Commun.*, 2015, **6**, 8654.
22 T. Jian, W. L. Li, X. Chen, T. T. Chen, G. V. Lopez, J. Li and L. S. Wang, *Chem. Sci.*, 2016, **7**, 7020.
23 W. L. Li, T. Jian, X. Chen, H. R. Li, T. T. Chen, X. M. Luo, S. D. Li, J. Li and L. S. Wang, *Chem. Commun.*, 2017, **53**, 1587.
24 M. Yan, H. R. Li, X. Y. Zhao, X. Q. Lu, Y. W. Mu, H. G. Lu and S. D. Li, *J. Comput. Chem.*, 2019, **40**, 966.
25 W. L. Li, L. Xie, T. Jian, C. Romanescu, X. Huang and L. S. Wang, *Angew. Chem.*, 2014, **126**, 1312.
26 W. L. Li, T. T. Chen, D. H. Xing, X. Chen, J. Li and L. S. Wang, *Proc. Natl. Acad. Sci. U. S. A.*, 2018, **115**, E6972.

27 X. Q. Lu, Q. Chen, X. X. Tian, Y. W. Mu, H. G. Lu and S. D. Li, *Nanoscale*, 2019, **11**, 21311.

28 T. T. Chen, W. L. Li, W. J. Chen, J. Li and L. S. Wang, *Chem. Commun.*, 2019, **55**, 7864.

29 T. T. Chen, W. L. Li, W. J. Chen, X. H. Yu, X. R. Dong, J. Li and L. S. Wang, *Nat. Commun.*, 2020, **11**, 2766.

30 H. Bai, Q. Chen, H. J. Zhai and S. D. Li, *Angew. Chem., Int. Ed.*, 2015, **54**, 941.

31 H. R. Li, X. X. Tian, X. M. Luo, M. Yan, Y. W. Mu, H. G. Lu and S. D. Li, *Sci. Rep.*, 2017, **7**, 5701.

32 Y. F. Zhao, X. Chen and J. Li, *Nano Res.*, 2017, **10**, 3407.

33 X. Chen, Y. F. Zhao, L. S. Wang and J. Li, *Comput. Theor. Chem.*, 2017, **1107**, 57.

34 D. J. Wales and J. P. Doye, *J. Phys. Chem. A*, 1997, **101**, 5111.

35 J. P. Perdew, K. Burke and M. Ernzerhof, *Phys. Rev. Lett.*, 1996, **77**, 3865.

36 C. Adamo and V. Barone, *J. Chem. Phys.*, 1999, **110**, 6158.

37 D. Feller, *J. Comput. Chem.*, 1996, **17**, 1571.

38 D. Andrae, U. Häußermann, M. Dolg, H. Stoll and H. Preuß, *Theor. Chim. Acta*, 1990, **77**, 123.

39 J. M. L. Martin and A. Sundermann, *J. Chem. Phys.*, 2001, **114**, 3408.

40 M. J. Frisch, *et al.*, *Gaussian 16, Revision A.03*, Gaussian Inc., Wallingford, CT, 2016.

41 A. D. Becke, *Phys. Rev. A: At., Mol., Opt. Phys.*, 1988, **38**, 3098.

42 J. P. Perdew, *Phys. Rev. B: Condens. Matter Mater. Phys.*, 1986, **33**, 8822.

43 T. H. Dunning Jr, *J. Chem. Phys.*, 1989, **90**, 1007.

44 R. A. Kendall, T. H. Dunning Jr and R. J. Harrison, *J. Chem. Phys.*, 1992, **96**, 6796.

45 J. Čížek, *Adv. Chem. Phys.*, 1969, **14**, 35.

46 G. D. Purvis and R. J. Bartlett, *J. Chem. Phys.*, 1982, **76**, 1910.

47 K. Raghavachari, G. W. Trucks, J. A. Pople and M. Head-Gordon, *Chem. Phys. Lett.*, 1989, **157**, 479.

48 P. E. D. Glendening, J. K. Badenhoop, A. E. Reed, J. E. Carpenter, J. A. Bohmann, C. M. Morales, C. R. Landis and F. Weinhold, *NBO 6.0*, Theoretical Chemistry Institute, University of Wisconsin, Madison, 2013.

49 D. Y. Zubarev and A. I. Boldyrev, *Phys. Chem. Chem. Phys.*, 2008, **10**, 5207.

50 N. V. Tkachenko and A. I. Boldyrev, *Phys. Chem. Chem. Phys.*, 2019, **21**, 9590.

51 J. VandeVondele, M. Krack, F. Mohamed, M. Parrinello, T. Chassaing and J. Hutter, *Comput. Phys. Commun.*, 2005, **167**, 103.

52 D. Geuenich, K. Hess, F. Köhler and R. Herges, *Chem. Rev.*, 2005, **105**, 3758.

53 Povray, *Persistence of vision raytracer, POV-Ray 3.7*, http://www.povray.org/.

54 S. Klod and E. Kleinpeter, *J. Chem. Soc., Perkin Trans. 2*, 2001, **2**, 1893.

55 E. Kleinpeter, S. Klod and A. Koch, *J. Mol. Struct.*, 2007, **811**, 45.

56 T. Lu and F. W. Chen, *J. Comput. Chem.*, 2012, **33**, 580.

57 R. Bauernschmitt and R. Ahlrichs, *Chem. Phys. Lett.*, 1996, **256**, 454.

58 P. Pyykkö and M. Atsumi, *Chem.–Eur. J.*, 2009, **15**, 186.

59 J. A. Dean, *Lange's Hand book of Chemistry*, McGraw-Hill Book Co., 1999, Table 4.6.

60 A. Tlahuice-Flores and A. Muñoz-Castro, *Int. J. Quantum Chem.*, 2019, **119**, e25756.

61 M. P. Johansson, *J. Phys. Chem. C*, 2009, **113**, 524.

62 G. J. Wang, M. F. Zhou, J. T. Goettel, G. J. Schrobilgen, J. Su, J. Li, T. Schlöder and S. Riedel, *Nature*, 2014, **514**, 475.

63 D. Ciuparu, R. F. Klie, Y. Zhu and A. L. Pfefferle, *J. Phys. Chem. B*, 2004, **108**, 3967.